IEEE Transactions on Robotics (T-RO) paper presented at
2024 IEEE/RSJ International Conference on Intelligent Robots and Systems (IROS)
October 14-18, 2024. Abu Dhabi, UAE

Design of an Adaptive Lightweight LiDAR to Decouple Robot-Camera Geometry

Yuyang Chen*[1], Dingkang Wang*[2], Lenworth Thomas[3], Karthik Dantu[1], Sanjeev J. Koppal[2,4]

***Abstract*—A fundamental challenge in robot perception is the coupling of the sensor pose and robot pose. This has led to research in active vision where robot pose is changed to reorient the sensor to areas of interest for perception. Further, egomotion such as jitter, and external effects such as wind and others affect perception requiring additional effort in software such as image stabilization. This effect is particularly pronounced in micro-air vehicles and micro-robots who typically are lighter and subject to larger jitter but do not have the computational capability to perform stabilization in real-time. We present a novel microelectromechanical (MEMS) mirror LiDAR system to change the field of view of the LiDAR independent of the robot motion. Our design has the potential for use on small, low-power systems where the expensive components of the LiDAR can be placed external to the small robot. We show the utility of our approach in simulation and on prototype hardware mounted on a UAV. We believe that this LiDAR and its compact movable scanning design provide mechanisms to decouple robot and sensor geometry allowing us to simplify robot perception. We also demonstrate examples of motion compensation using IMU and external odometry feedback in hardware.**

I. Introduction

Modern autonomy is largely driven by vision and depth sensors for perception. Most such techniques make an implicit assumption that the relative pose of the sensor w.r.t. the robot is fixed and changes in sensor viewpoint require a change in the robot pose. This implies that fast-moving robots must deal with motion compensation (i.e. camera-robot *stabilization*) and that robots need to reorient themselves to observe the relevant parts of the scene. Correspondingly, stabilization [19, 5, 24, 21] and active vision [4, 2, 34, 22] are well-studied problems.

Let us consider the specific example of image stabilization. While successful, most such methods compensate through *post-capture* processing of sensor data. *We contend that this is simply not feasible for the next generation of fast miniature robots* such as robotic bees [30], crawling and walking robots [11], and other micro-air vehicles [18]. For example, flapping-wing robots such as the RoboBee exhibit a high frequency rocking motion (at about 120 Hz in one design) due to the piezo-electric actuation [10]. Environmental factors such as wind affects micro-robots to a greater extent than a larger robot. There might be aerodynamic instability due to ornithopter-based shock absorption [31]. The egomotion of small robots (and onboard sensors) is quite extreme making any sensing challenging. While there have been software methods to correct for such effects for cameras [3] and LiDARs [20], this is often difficult to perform in real-time onboard due to the computational, energy and latency constraints on the robot mentioned above. Without proper motion compensation for miniature devices, we will not be able to unlock the full potential of what is one of the ten grand challenges in robotics [32].

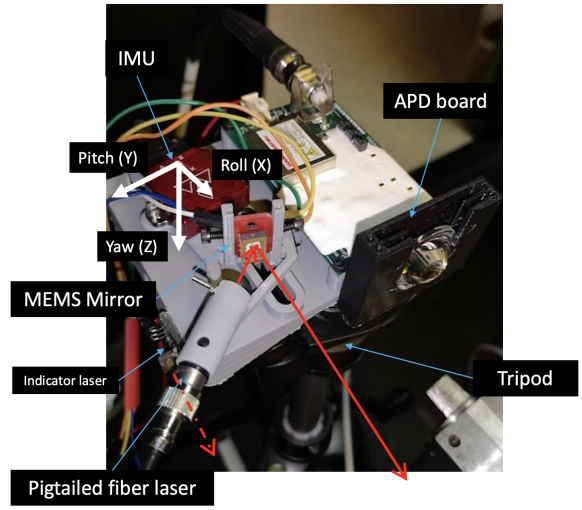

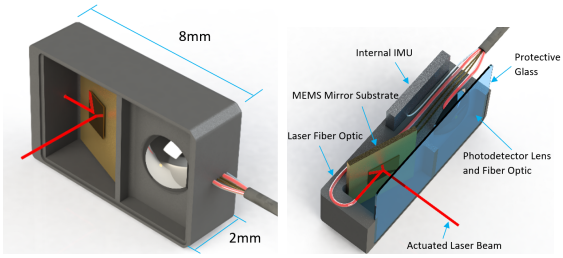

Fig. 1: Our design is given above with the prototype motion-compensated LiDAR (up), and we also prepared a design for future work to integrate this onto smaller platforms.

A. *Key Idea: Compensation* during *Imaging*

Our idea is for motion correction to happen in sensor hardware during imaging such that measurements are already

[1]Yuyang Chen and Karthik Dantu are with the Department of Computer Science and Engineering, University at Buffalo, Buffalo, NY 14260, USA yuyangch@buffalo.edu, kdantu@buffalo.edu

[2,3]Dingkang Wang and Sanjeev Koppal are with the Department of Electrical and Computer Engineering; Lenworth Thomas is with the Department of Mechanical and Aerospace Engineering, University of Florida, Gainesville, FL 32603, USA noplaxochia@ufl.edu, sjkoppal@ece.ufl.edu, lenworth.thomas@ufl.edu

[4] Sanjeev J. Koppal holds concurrent appointments as an Associate Professor of ECE at the University of Florida and as an Amazon Scholar at Amazon Robotics. This paper describes work performed at the University of Florida and is not associated with Amazon.

*Equal contributions.

(a) start of video (b) midway (c) end

(d) Average of all images in video

Fig. 2: Biological motion compensation. The position and the angle of the head of the hawk remain stable despite body motion to provide the hawk an stabilized vision. https://www.youtube.com/watch?v=aqgewVCC0k0

compensated without requiring onboard computing. This paper shows the motion compensation advantage of decoupling robot-camera geometry, and providing the ability to control the camera properties independent of the robot pose could bring about a new perspective to robot perception and simplify the autonomy pipeline. We demonstrate this through the design of a MEMS-driven LiDAR and perform compensation in two ways - (i) onboard IMU, and (ii) external feedback of robot pose at a high rate.

We are inspired by animal eyes that have fast mechanical movements that compensate for motion, in real-time and at high accuracy [1]. In Fig. 2, we show frames $V(t)$ from a video of a hawk (*Buteo jamaicensis*) being moved by a human trainer [8]. We also show the average of the video $\sum_t \frac{V(t)}{T}$ over a time interval T. Note that the averaged image shows motion blurring, except where the eagle mechanically compensates for the shifts. We envision biologically-inspired motion compensation that happens during sensing. These sensors need to adaptively change their orientation, in real-time, and in concert with robot goals such as mapping or navigation. Effectively, the rotation matrix R must cancel out robot motion to provide a "stable" view of a scene.

B. MEMS Mirror-enabled Adaptive LIDAR

The ability to reorient sensor pose could have many uses in robotics, particularly in image alignment during motion such as in SLAM. If the camera and robot are rigidly attached, then the camera experiences all the motion the robot experiences, including jitter and other potential disturbances that are detrimental to the Visual SLAM task. This could result in spurious features, errors in localization, and incorrect feature association leading to an inaccurate map. In this paper, we describe a sensor design that can perform image reorientation of a LiDAR in hardware without the need for any software processing for such compensation. Previously, pan-tilt-zoom (PTZ) cameras have attempted to address this problem. However, they use mechanical actuation which can react in ones of Hz making it not suitable for tasks such as egomotion compensation in real-time. This is evidenced by the limited use of PTZ cameras on robots - most robots just have sensors rigidly attached.

Our designs break through these past difficulties by exploiting recently available microelectromechanical (MEMS) and opto-mechanical components for changing camera parameters. Opto-MEMS components are famously fast (many kHz), and they allow the changing of the LiDAR projection offset orientation during robot motion, such that the view of LiDAR is effectively static. By changing LiDAR views two orders of magnitude (or more) faster than robot motion, we can effectively allow for camera views to be independent of the robot view. In this work, we can compensate the LiDAR point cloud using an onboard IMU or external feedback such as motion tracking setup. More generally, such compensation allows the robot to focus on the control task while the camera can perform perception (which is required for the control task) independently, and greatly simplifies robot planning as the planner does not need to account for perception and just needs to reason about the control task at hand.

II. Contributions

MEMS LiDAR optics have the advantages of small size and low power consumption [25, 14, 15]. Our algorithmic and system design contributions beyond this are:

- We present the design of a novel LiDAR sensor adopting a MEMS mirror similar to this LiDAR MEMS scanner [28]. This design enables wide non-resonant scanning angles for arbitrary orientations. We integrate this with two types of feedback (IMU and external sensors) to demonstrate quick and high-rate motion compensation. Fig. 1 shows the design of our sensor.
- We present the compensation control algorithms for our LiDAR. We further characterize the performance of compensation control through experiments and simulations in Sec. IV.
- We show UAV flight with a proof-of-concept hardware prototype combining external feedback with the MEMS mirror for egomotion compensation. We enable UAV flight by tethering the MEMS modulator to the other heavy necessary components, like the laser, photodetector, optics, the driver circuit, and the signal processing circuitry. The frequencies of the mirror modulation and IMU measurement are much higher than typical robot egomotion. Our prototype MEMS compensated scan system can perform such compensation in under 10 ms. Please see the accompanying video for proper visualization, and see Fig. 5.

III. Related Work

Small, compact LiDAR for small robotics: MEMS mirrors have been studied to build compact LiDAR systems [25, 14].
software-based compensation: Software-based compensation for robotics motion has been studied in great detail in SLAM algorithms [24] or expectation-maximization (EM) methods[21]. Software-based motion compensation have a relative high computation barrier for micro-robotics and may degrade if the point cloud have large discrepancy.
Motorized gimbals: Comparing to motorized image stabilization systems [13], MEMS mirrors not only have smaller size and lighter weight, but their frequency response bandwidth are better than the bulky and heavy camera stabilizer.
Motion compensation in displays and robotics: Motion-compensated MEMS mirror scanner has been applied for projection, [6], where hand-shake is an issue. In contrast, we deal with the vibration of much higher frequencies, and our approach is closest to adaptive optics for robotics. For example, [23] change the zoom and focal lengths of cameras for SLAM. Our prior work [25] changed zoom in LiDARs. In this work, we compensate using small mirrors, utilizing a rich tradition of compensation in device characterization[16] and to improve SNR [9]. Compared to all the previous methods, we are the first to show IMU-based LiDAR compensation with a MEMS mirror in hardware.

IV. Method: Novel LiDAR Design

We propose a simple and effective design, where the MEMS mirror and photodetector are placed on a movable head. For image stabilization, we are also able to place the IMU there. A LiDAR engine and accompanying electronics are tethered to this device, which can be light and small enough for micro-robots. To enable both the LiDAR scanning and compensated scanning at high rate, it is important to understand the characterization of the MEMS scanner.

A. The MEMS mirror

All the compensation effects and size advantages described so far will be nullified if the MEMS mirror cannot survive the shock, vibration and shake associated with real-world robots. Here we analyze the robustness of the MEMS mirror device for such platforms. Most MEMS mirrors rely on high-quality factor resonant scanning to achieve wide field-of-view (FoV), which leads to heavy ringing effects and overshoot with sudden changes of direction [17, 26]. A suitable MEMS mirror for motion-compensated scanning is expected to have a wide non-resonant scanning angle, smooth and fast step responses, can operate under common robotics vibration and can survive shock. To achieve this goal, we adopt a popular electrothermal bimorph actuated MEMS mirror design [12, 27] to build this MEMS mirror. The employed MEMS mirror is fabricated with Al/SiO_2 based inverted-series-connected (ISC) bimorph actuation structure reported in [12]. This type of MEMS mirror has the advantages of simple and mature fabrication process [33, 29], wide non-resonant scanning angle, linear response and good stiffness. A new electrothermal MEMS mirror is designed and fabricated with the adaption of the motion compensation application. We note that other previously reported MEMS mirrors with electrothermal actuators, electrostatic actuators, or electromagnetic actuators may also be applicable to the motion compensated LiDAR scanning [14, 28].

B. Compensation Algorithm

In the previous sections, we saw the advantages of MEMS mirror-based compensation and the feasibility for use in a robotic LiDAR. Here we focus on the details of the hardware-based rotation compensation algorithm using MEMS mirror scanning LiDAR and sensing for the compensation.

The MEMS mirror reflect a single ray of light towards a point in the spherical coordinate $\{\alpha, \beta, r\}$. The $\{\alpha, \beta\}$ are the two angular control input to the mirror to achieve such target. We will first establish the local(robot) and global (world) frames, then introduce known helper conversion from spherical to Cartesian coordinates, and finally gets into the details of compensation.

1) Preliminaries:

a) Coordinate System: Our LiDAR can compensate for rotation, but it can not compensate for translation. So all discussion heres on in drops the translation from $SE(3)$ and will only be focus on $SO(3)$. Let the robot have rotation $\boldsymbol{R}^w_{robot} \in SO(3)$ relative to the world frame. In here, the frame of the un-moving base of the LiDAR sensor have Identity rotation $\boldsymbol{R}^w_{base} \in SO(3)$ and therefore identical $SO(3)$ transformation as the robot frame.

b) Spherical-to-Cartesian Conversions: It is important to outline the conversion from the spherical, which is the control coordinate, to normal Cartesian coordinate. Points in the spherical coordinate $\{\alpha, \beta, r\}$ can be converted to Cartesian coordinate via known equations,

$$p_{cartesian} = \begin{bmatrix} x \\ y \\ z \end{bmatrix} = \begin{bmatrix} r\cos\alpha\cos\beta \\ r\cos\alpha\sin\beta \\ r\sin\alpha \end{bmatrix} \tag{1}$$

and vice versa:

$$p_{spherical} = \begin{bmatrix} \alpha \\ \beta \\ r \end{bmatrix} = \begin{bmatrix} \arctan\frac{z}{\sqrt{x^2+y^2}} \\ \arctan\frac{y}{x} \\ \sqrt{x^2+y^2+z^2} \end{bmatrix} \tag{2}$$

Note that both $p_{cartesian}$ and $p_{spherical}$ are points located in the robot's local coordinate frame, $\boldsymbol{R}^w_{robot}$. Other literature's refer to this frame as the local frame, or camera frame.

c) Spatial Scanning: A set of i spherical control coordinates $\{\alpha_i, \beta_i, r_i\}$ defines the scanning pattern of the LiDAR. We use $r_i = 1$ for unit length vectors. In our setup, $\{\alpha_i, \beta_i\}$ defines a rectangular scanning grid in the spherical coordinate, whose center is the principle axis. See figure 3a. Within this limit, the mirror can direct its beam to any point desired by the user.

d) Desired Sensor World Frame Rotation: In our design, users can define a desired world frame rotation of the sensor, separately from the world frame rotation of the robot. The rotational decoupling of a sensor and a robot provides many benefits which we demonstrate through various application in

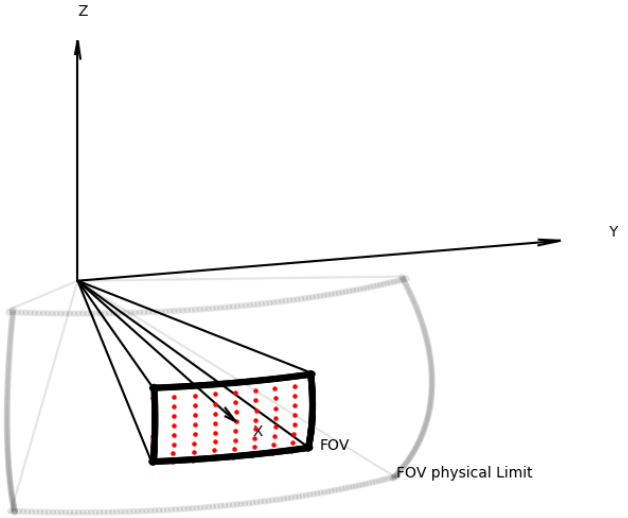

(a) Depicting Spatial Scanning Grid in the sensor's base frame. In the real sensor, the resolution of the scanning grid is higher at 20x20. The input rotation here is zero. In other words, $\boldsymbol{R}_{control} = \boldsymbol{I}$.

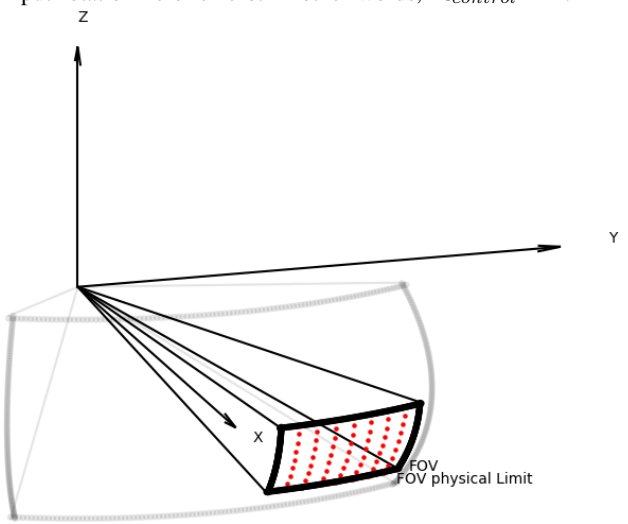

(b) Depicting Spatial Scanning Grid in the sensor's base frame, The input rotation is none-zero here.

Fig. 3

this work. Let $\boldsymbol{R}^w_{desired} \in SO(3)$ be the desired rotation target in the world frame. $\boldsymbol{R}^w_{desired}$ can be decided by the users. For example, it can be a slower changing rotation, relative to the robot's body frame.We will touch on the exact details later in IV-B4. Other possibility includes aiming towards a specific world frame target $t \in \mathbb{R}^3$ which we will touch on later, in IV-B5.

2) General Rotation Compensation: Given robot world frame rotation $\boldsymbol{R}^w_{robot}$, user desired sensor rotation $\boldsymbol{R}^w_{desired}$ and a set of spatial scanning, spherical, sensor input coordinates $\{\alpha_i, \beta_i, r_i\}$, we need to find the adjusted sensor input coordinates $\{\alpha_i^*, \beta_i^*, r_i^*\}$, in order to achieve user desired sensor rotation $\boldsymbol{R}^w_{desired}$. We will outline the calculations step by step.

a) Step1: we first translate each $\{\alpha_i, \beta_i, r_i\}$ to Cartesian $p_{cartesian}$ by Eq. 1. This step is necessary, in order to calculate points transformation with rotation matrices.

b) Step2: The control rotation input to the sensor $\boldsymbol{R}_{control}$, is the difference between the desired world frame sensor rotation $\boldsymbol{R}^w_{desired}$ and the robot's current world frame rotation $\boldsymbol{R}^w_{robot}$.

Put it formally, Let $\boldsymbol{R}_{control}$ be the rotation from robot rotation $\boldsymbol{R}^w_{robot}$ to the desired rotation $\boldsymbol{R}^w_{desired}$, therefore $\boldsymbol{R}^w_{desired} = \boldsymbol{R}_{control}\boldsymbol{R}^w_{robot}$. We have,

$$\boldsymbol{R}_{control} = \boldsymbol{R}^w_{desired}(\boldsymbol{R}^w_{robot})^T \tag{3}$$

Intuitively, When there is no difference between the desired sensor rotation and the robot rotation, where $\boldsymbol{R}^w_{desired} = \boldsymbol{R}^w_{robot}$ then $\boldsymbol{R}_{control} = \boldsymbol{R}^w_{desired}(\boldsymbol{R}^w_{desired})^T = \boldsymbol{I}$. And $\{\alpha_i, \beta_i, r_i\} = \{\alpha_i^*, \beta_i^*, r_i^*\}$ This default orientation is shown in figure 3a. When there is a difference however, an example is shown in Figure 3b.

c) Step3: Now, all points in the spatial scanning pattern $p_{cartesian} = \{x_i, y_i, z_i\}$ of the robot frame $\boldsymbol{R}^w_{robot}$ can be transformed to have the desired sensor world frame rotation $\boldsymbol{R}^w_{desired}$,:

$$p_{desired-cartesian} = \boldsymbol{R}_{control}p_{cartesian} \tag{4}$$

substituting $\boldsymbol{R}_{control}$, we have

$$p_{desired-cartesian} = \boldsymbol{R}^w_{desired}(\boldsymbol{R}^w_{robot})^T p_{cartesian} \tag{5}$$

d) Step4: Finally, we can translate the rotated points $p_{desired-cartesian_i}$ back to the spherical coordinate $p_{desired-spherical_i}$, via Eq. 2 for point i's rotation control input to the sensor. Now that we have come to our answer for $\{\alpha_i^*, \beta_i^*, r_i^*\}$.

It is important to note that, this full $SO(3)$ compensation is only achievable because our LiDAR project individual point p_i independently from other points in the set. In the case of a traditional camera or a commercially available LiDAR like Velodyne, The entire set of p_i can be viewed as being projected as a group and correlate to each other. In these other sensors, Full $SO(3)$ compensation is not achievable, even if the sensors are mounted to the robot by a universal joint with 2 degree-of-freedoms α, β. But we will also analyze this special case of grouped points re-projection since our LiDAR can achieve this 2-axis-only compensation.

3) Special Case: 2-axes only compensation: It is important to analyze the case where the sensor can only rotate in two axes relative to the robot. Such setup is commonly seen in robots with cameras mounted by a 2-axis gimbal, as well as PTZ cameras. Another applicable scenario is when we mount a commercially available Velodyne on a UAV via a universal joint, to perform LiDAR SLAM studies and design motion-compensated LiDAR SLAM. Furthermore, when it comes to the target aiming IV-B5, 2-axis rotation is often preferred. Our sensor can perform such compensation as well.

In this subsection, we will outline the control not only for our sensor but all sensors, that mount on robots via joints or gimbals with 2-axis orientation controls.

In IV-B2b we define $\boldsymbol{R}_{control}$ as the difference between the sensor orientation and the robot's orientation. Since $\boldsymbol{R}_{control} \in SO(3)$ it requires at least 3-axis rotation control to achieve.

We can collapse this $\boldsymbol{R}_{control}$ matrix into a rotation matrix that is the composition of two Euler angles. The new rotation matrix will not be identical to $\boldsymbol{R}_{control}$, but it keeps the same sensor principle axis ray direction. We herein refer to the collapsed version as $\boldsymbol{R}^*_{control}$.

Let $\boldsymbol{R}_{control}$ be limited to 2-axes rotation only:

$$\boldsymbol{R}^*_{control} = \begin{bmatrix} \cos\beta & -\sin\beta & 0 \\ \sin\beta & \cos\beta & 0 \\ 0 & 0 & 1 \end{bmatrix} \begin{bmatrix} \cos\alpha & 0 & \sin\alpha \\ 0 & 1 & 0 \\ -\sin\alpha & 0 & \cos\alpha \end{bmatrix} \tag{6}$$

Here is how to find $\boldsymbol{R}^*_{control}$ from a given $\boldsymbol{R}_{control}$, step by step.

a) Step1: Rotate the principle axis $\boldsymbol{e}_1$, with $\boldsymbol{R}_{control}$ in our case $\boldsymbol{e}_1 = \{x = 1, y = 0, z = 0\}^T$.

$$\boldsymbol{e}_{rotated} = \boldsymbol{R}_{control}\boldsymbol{e}_1 \tag{7}$$

$\boldsymbol{e}_{rotated}$ is now the new principle axis that our sensor should target. Note that, $\boldsymbol{e}_{rotated}$ is closely related to the ray vector from robot to target in the aiming application, more on this later at IV-B5.

b) Step2: We then translate this Cartesian coordinate $\boldsymbol{e}_{rotated}$ vector into the Spherical coordinate, using Eq. 2. We will get $\{\alpha, \beta, 1\}$.

c) Step3: Finally, we can use Eq. 6 to find the collapsed $\boldsymbol{R}^*_{control}$ with α, β.

Our LiDAR can then use $\boldsymbol{R}^*_{control}$ to perform 2-axis only compensation. We can simply follow the same steps in IV-B2, except we replaces $\boldsymbol{R}_{control}$ in Eq. 4 with $\boldsymbol{R}^*_{control}$.

Further, this compensation can be readily extended to commercially available cameras and LiDARs (such as Velodyne) mounted on a universal joint to the robot frame or a 2-axis gimbal-mounted camera. The 2-axis angles α, β are enough to describe the two joint rotations.

4) Rotational FoV Stabilization: It is often desirable to have relatively slow rotating sensor world frame FoV in many SLAM related applications. In here we go into details of how it is achieved with our sensor.

a) Quaternion $L_2 - mean$: Supposedly $q_1.....q_n$ is the world frame quaternions store in a queue data structure, representing the robot's world frame rotation in the last n time stamps. We can find its average via LERP, summing and normalizing the quaternions as 4-vectors [7]:

$$q_{avg} = \frac{\sum_{i=1}^{n} q_i}{||\sum_{i=1}^{n} q_i||_2} \tag{8}$$

q_{avg} can be converted into a rotation matrix $\boldsymbol{R}^w_{desired}$. Along with the robot's current world frame rotation $\boldsymbol{R}^w_{robot}$, we can find the adjusted spherical coordinate control input to our sensors $\{\alpha^*_i, \beta^*_i, r^*_i\}$, according to IV-B2.

5) Target Aiming: Let $t^w_{target} \in \mathbb{R}^3$ be the target of interest in the world frame, and let t^w_{robot} be the robot's current world frame translation. Then

$$p_{aim} = (\boldsymbol{R}^w_{robot})^T(t^w_{target} - t^w_{robot}) \tag{9}$$

outlines the ray direction which we want to align our "principle axis", or the projection center point towards. Following a very similar process as to IV-B3 we can find the controls:

a) Step1: We can simply translate Cartesian coordinate p_{aim} to spherical coordinate via Eq. 2 to find α, β.

b) Step2: Then compose a $\boldsymbol{R}^*_{control}$ via Eq. 6 for the entire scanning grid. We can simply follow the same steps in IV-B2, except we replaces $\boldsymbol{R}_{control}$ in Eq. 4 with $\boldsymbol{R}^*_{control}$

For all other sensors mounted on 2-axis gimbals or universal joints, α, β is enough to describe the joint inputs.

6) MEMS Related details: MEMS-related details, relating to the 1-dimension controls of each actuation axis $\{\alpha, \beta\}$, including analysis of robot motion shock on the MEMS as well as preliminary pointcloud stitching, are included in the appendix.

C. LiDAR Hardware Specifics

Our prototype (Fig. 4) uses an InGaAs avalanche photodiode module (Thorlabs, APD130C). A fiber with a length of 3 m delivers the laser from the laser source to the scanner head. The gain-switch laser (Leishen, LEP-1550-600) is collimated and reflected by the MEMS mirror. The X-axis of the IMU (VectorNav, VN-100) is parallel to the neutral scanning direction of the MEMS mirror. The in-run bias stability of the gyroscope is $5 - 7°$/hr typ. The scanner head sits on a tripod so that it can be rotated in the yaw and pitch directions. In the LiDAR base, an Arduino microcontroller is used to process the time-of-flight (ToF) signals, sample the IMU signals and control the MEMS mirror scanning direction. The data are sent to a PC for post-processing and visualization.

Since our motivation was to use micro-robots, our maximum detection distance is 4 m with a 80% albedo object and the minimal resolvable distance is 5 cm. The maximum ToF measurement rate is 400 points/sec. According to the compensation algorithm described in the previous section, the MEMS mirror scanning direction is updated and compensated for motion at 400 Hz. We now describe our experiments. Please see the accompanying video for further clarification.

V. UAV Experiment

Next, we demonstrated the motion compensated LiDAR by flying it on a UAV. The robot pose is from an external motion capture system that tracks the UAV. We vary the robot pose sampling rate and study its effect on the effect of compensation. The UAV is controlled to hover at a designated position with yaw/pitch rotation as motion jitter. Motion compensated LiDAR is set to compensate all the rotational motion, including the controlled rotation and the random motion disturbance. The compensated MEMS scanning laser uses a visible light, and the other visible laser is fixed at a relative higher position on the UAV, as shown in the images in Fig. 5b. The target scanning direction is a fixed point on the target.

Here, the entire scanning grid $\{\alpha_i, \beta_i, 1\}$ consist of 20x20 grid pattern points. We use the aiming compensation outline in IV-B5

We trim about 12 s videos in each experiments while the UAV is flying, and then each frames of the videos are accumulated into an image to track the motion of the UAV and the errors of the compensated scanning.

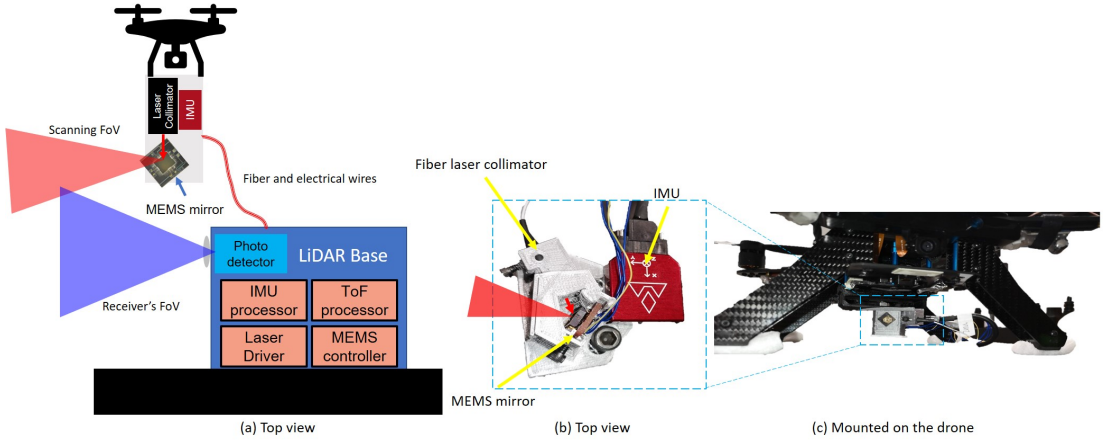

Fig. 4: The movable LiDAR MEMS scanner head, which include the MEMS mirror, an IMU and a fiber laser collimator. (a) shows the top view and (b) shows the LiDAR scanner head mounted to the bottom of the UAV.

The robot pose sampling rate is set from 1 Hz to 200 Hz to investigate its effect on the compensation results. The controlled UAV rotations are in the yaw and pitch direction. However, the actual motions cause some random motions during the flying. Point clouds are also collected when the UAV is hovering and we overlap several frames. As the robot pose sampling frequency increases from 1Hz, 2Hz to 50Hz, the width of the overlapping area shrink from 10 to 11 points at 1Hz (Fig. 6f), to 6 points at 50 Hz (6d). As Fig. 14 demonstrated, the compensation frequency has clear impacts on the quality of the captured point-cloud.

VI. Conclusions

We have designed an adaptive lightweight LiDAR capable of reorienting itself. We have demonstrated the benefits of such a LiDAR in simulation as well as experiment. We have demonstrated in experiment image stabilization in hardware using an onboard IMU. We have also demonstrated viewing an object of interest using this LiDAR through external robot pose feedback.

References

[1] Thiemo Alldieck et al. "Optical flow-based 3d human motion estimation from monocular video". In: *German Conference on Pattern Recognition*. Springer. 2017, pp. 347–360.

[2] Andreas Bircher et al. "Receding horizon" next-best-view" planner for 3d exploration". In: *2016 IEEE international conference on robotics and automation (ICRA)*. IEEE. 2016, pp. 1462–1468.

[3] Chao-Ho Chen et al. "Real-time video stabilization based on motion compensation". In: *2009 Fourth International Conference on Innovative Computing, Information and Control (ICICIC)*. IEEE. 2009, pp. 1495–1498.

[4] Gabriele Costante et al. "Perception-aware Path Planning". In: *IEEE Transactions on Robotics* (2016), Epub–ahead.

[5] Zan Gojcic et al. "The perfect match: 3d point cloud matching with smoothed densities". In: *Proceedings of the IEEE/CVF Conference on Computer Vision and Pattern Recognition*. 2019, pp. 5545–5554.

[6] Heinrich Grüger et al. "3.1: MOEMS Laser Projector for Handheld Devices Featuring Motion Compensation". In: *SID Symposium Digest of Technical Papers*. Vol. 38. 1. Wiley Online Library. 2007, pp. 1–3.

[7] Richard Hartley et al. "Rotation averaging". In: *International journal of computer vision* 103.3 (2013), pp. 267–305.

[8] *Hawk Head Stabilization*. Jan. 2020. URL: https://www.youtube.com/watch?v=aqgewVCC0k0.

[9] Tomohiko Hayakawa et al. "Gain-compensated sinusoidal scanning of a galvanometer mirror in proportional-integral-differential control using the pre-emphasis technique for motion-blur compensation". In: *Applied Optics* 55.21 (2016), pp. 5640–5646.

[10] E Farrell Helbling, Sawyer B Fuller, and Robert J Wood. "Pitch and yaw control of a robotic insect using an onboard magnetometer". In: *2014 IEEE international conference on robotics and automation (ICRA)*. IEEE. 2014, pp. 5516–5522.

[11] Katie Lynn Hoffman. "Design and locomotion studies of a miniature centipede-inspired robot". PhD thesis. 2013.

[12] Kemiao Jia, Sagnik Pal, and Huikai Xie. "An electrothermal tip–tilt–piston micromirror based on folded dual S-shaped bimorphs". In: *Journal of Microelectromechanical systems* 18.5 (2009), pp. 1004–1015.

[13] Ruting Jia et al. "System performance of an inertially stabilized gimbal platform with friction, resonance, and vibration effects". In: *Journal of Nonlinear Dynamics* 2017 (2017).

[14] Abhishek Kasturi et al. "UAV-borne lidar with MEMS mirror-based scanning capability". In: *Laser Radar Technology and Applications XXI*. Vol. 9832. International Society for Optics and Photonics. 2016, p. 98320M.

(a) Our UAV setup with Intel Aero UAV and our LiDAR mounted on it.

(b) Effect of compensation rate on yaw rotation

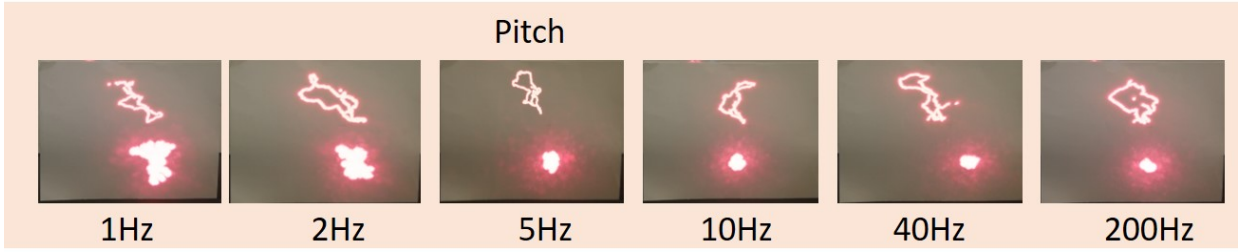

(c) Effect of compensation rate on pitch rotation

Fig. 5: A comparison of the compensation strength versus the robot pose sampling frequencies. All the images are accumulation of 12s of UAV hovering videos. The compensation target scanning direction is a fixed direction.

[15] Katsumi Kimoto et al. “Development of small size 3D LIDAR”. In: *2014 IEEE International Conference on Robotics and Automation (ICRA)*. IEEE. 2014, pp. 4620–4626.

[16] Ievgeniia Maksymova et al. “Detection and Compensation of Periodic Jitters of Oscillating MEMS Mirrors used in Automotive Driving Assistance Systems”. In: *2019 IEEE Sensors Applications Symposium (SAS)*. IEEE. 2019, pp. 1–5.

[17] Veljko Milanović et al. “Closed-loop control of gimbal-less MEMS mirrors for increased bandwidth in LiDAR applications”. In: *Laser Radar Technology and Applications XXII*. Vol. 10191. International Society for Optics and Photonics. 2017, 101910N.

[18] Yash Mulgaonkar, Gareth Cross, and Vijay Kumar. “Design of small, safe and robust quadrotor swarms”. In: *2015 IEEE international conference on robotics and automation (ICRA)*. IEEE. 2015, pp. 2208–2215.

[19] Frank Neuhaus et al. “Mc2slam: Real-time inertial lidar odometry using two-scan motion compensation”. In: *German Conference on Pattern Recognition*. Springer. 2018, pp. 60–72.

[20] Tao Peng and Satyandra K Gupta. “Model and algorithms for point cloud construction using digital projection patterns”. In: (2007).

[21] Ethan Phelps and Charles A Primmerman. “Blind Compensation of Angle Jitter for Satellite-Based Ground-

(a) Our set up with UAV, LiDAR and the feature target.

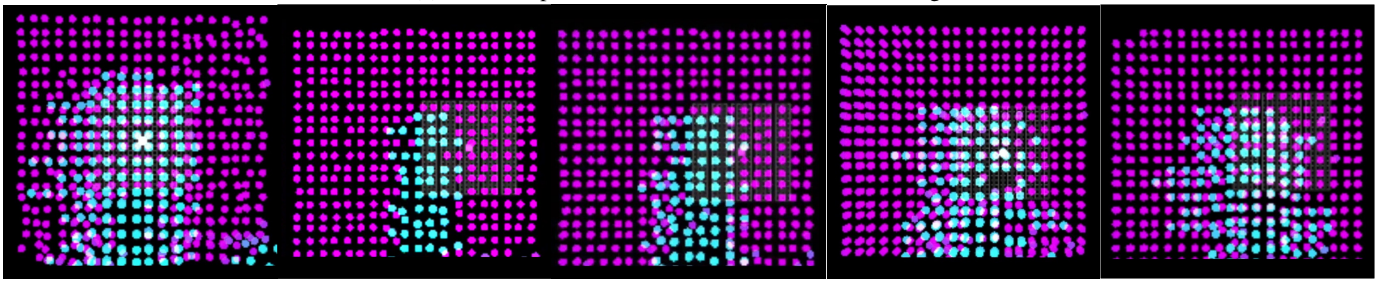

(b) Uncompensated (c) One frame (d) 50Hz sampling rate (e) 2Hz sampling rate (f) 1Hz sampling rate

Fig. 6: A comparison of the compensation strength verse the IMU sampling frequencies. The images are accumulation of 20s of point cloud video during the UAV hovering. We use a cuboidal object (as seen in Fig. 6a) as object of interest. The width of the target increases due to compensation inaccuracy as we reduce compensation rate from 50 Hz to 1 Hz demonstrating the utility of high rates of compensation even in such static scenarios

Imaging Lidar". In: *IEEE Transactions on Geoscience and Remote Sensing* 58.2 (2019), pp. 1436–1449.

[22] Seyed Abbas Sadat et al. "Feature-rich path planning for robust navigation of MAVs with mono-SLAM". In: *2014 IEEE International Conference on Robotics and Automation (ICRA)*. IEEE. 2014, pp. 3870–3875.

[23] Takafumi Taketomi and Janne Heikkilä. "Zoom factor compensation for monocular SLAM". In: *2015 IEEE Virtual Reality (VR)*. IEEE. 2015, pp. 293–294.

[24] Takafumi Taketomi, Hideaki Uchiyama, and Sei Ikeda. "Visual SLAM algorithms: a survey from 2010 to 2016". In: *IPSJ Transactions on Computer Vision and Applications* 9.1 (2017), p. 16.

[25] Zaid Tasneem et al. "Adaptive fovea for scanning depth sensors". In: *The International Journal of Robotics Research* 39.7 (2020), pp. 837–855.

[26] Dingkang Wang, Connor Watkins, and Huikai Xie. "MEMS Mirrors for LiDAR: A review". In: *Micromachines* 11.5 (2020), p. 456.

[27] Dingkang Wang et al. "A Large Aperture 2-Axis Electrothermal MEMS Mirror for Compact 3D LiDAR". In: *2019 International Conference on Optical MEMS and Nanophotonics (OMN)*. IEEE. 2019, pp. 180–181.

[28] Dingkang Wang et al. "A low-voltage, low-current, digital-driven MEMS mirror for low-power LiDAR". In: *IEEE Sensors Letters* 4.8 (2020), pp. 1–4.

[29] Dingkang Wang et al. "An ultra-fast electrothermal micromirror with bimorph actuators made of copper/tungsten". In: *2017 International Conference on Optical MEMS and Nanophotonics (OMN)*. IEEE. 2017, pp. 1–2.

[30] Robert Wood, Radhika Nagpal, and Gu-Yeon Wei. "flight of the robobees". In: *Scientific American* 308.3 (2013), pp. 60–65. ISSN: 00368733, 19467087. URL: http://www.jstor.org/stable/26018027.

[31] Dong Xue et al. "Computational simulation and free flight validation of body vibration of flapping-wing MAV in forward flight". In: *Aerospace Science and Technology* 95 (2019), p. 105491.

[32] Guang-Zhong Yang et al. "The grand challenges of Science Robotics". In: *Science robotics* 3.14 (2018), eaar7650.

[33] Xiaoyang Zhang, Liang Zhou, and Huikai Xie. "A fast, large-stroke electrothermal MEMS mirror based on Cu/W bimorph". In: *Micromachines* 6.12 (2015), pp. 1876–1889.

[34] Zichao Zhang and Davide Scaramuzza. "Perception-aware receding horizon navigation for MAVs". In: *2018 IEEE International Conference on Robotics and Automation (ICRA)*. IEEE. 2018, pp. 2534–2541.